



## 3D Integrated numerical model for fluid–structures–seabed interaction (FSSI): Elastic dense seabed foundation



Ye Jianhong<sup>a,\*</sup>, D.-S. Jeng<sup>b</sup>, A.H.C. Chan<sup>c</sup>, R. Wang<sup>a</sup>, Q.C. Zhu<sup>a</sup>

<sup>a</sup> State Key Laboratory of Geomechanics and Geotechnical Engineering, Institute of Rock and Soil Mechanics, Chinese Academy of Sciences, Wuhan 430071, China

<sup>b</sup> Griffith School of Engineering, Griffith University, Gold Coast, Queensland 4222, Australia

<sup>c</sup> School of Engineering and Information Technology, Federation University of Australia, Ballarat 3353, Australia

### ARTICLE INFO

#### Article history:

Received 25 December 2014

Accepted 8 January 2016

#### Keywords:

Fluid–structures–seabed interaction (FSSI)

Poro-elastic seabed foundation

Dynamics of offshore structures

3D momentary liquefaction

Caisson breakwater

FSSI-CAS 3D

### ABSTRACT

Economic losses and property damage due to the failure of offshore structures are huge each year in the world, under the attack of endless conventional wave, occasional tropical storms or typhoons, and possible tsunami. Wave-induced dynamics of offshore structures and their seabed foundation attract a great deal of attention from researchers and ocean engineers. Previous literature investigated the wave–structures–seabed interaction generally adopting 2D models and decoupled way. In this study, taking a caisson breakwater as the typical offshore structure, the simple linear interaction between ocean wave, a caisson breakwater and its poro-elastic seabed foundation is investigated by utilizing a three-dimensional integrated numerical model FSSI-CAS 3D. The numerical results indicate that FSSI-CAS 3D can effectively and sufficiently capture a variation of phenomena of wave-induced dynamics of offshore structures, and momentary liquefaction in its dense poro-elastic seabed foundation. This study demonstrates great promise of using the developed integrated numerical model in offshore industry to predict the dynamic response and stability of offshore structures by ocean engineers in design stage.

© 2016 Elsevier Ltd. All rights reserved.

### 1. Introduction

In the past two decades, a great number of marine structures, such as breakwater, pipeline, offshore wind turbine and oil platform, were constructed in offshore area for a variation of special purposes, for example, breakwater is for port protection or sediment transport regulation; wind turbine is to harvest offshore renewable energy. Comparing with structures built on land, offshore structures are much easier to lose their stability due to the environment loading, and their vulnerable saturated or nearly saturated seabed foundation. It is well known that offshore structures generally are applied by endless conventional ocean wave, occasional tropical storms or typhoons, possible seismic wave and related earthquake triggered tsunami. Furthermore, soil liquefaction is easy to occur in saturated or nearly saturated seabed foundation under ocean wave or seismic wave loading. There have been some reports about the wave-induced failure of offshore structures in previous literatures, for example, Franco (1994), Zhang and Ge (1996), and Chung et al. (2006). According to the official statistics, the total length of failed offshore breakwater

in each year due to the attack of tropical storms and typhoons in China reaches up to 40 km. Most recently, the deep water breakwater in a military vessels port located at Sanya city, south of China, is seriously damaged when the super typhoon “Butterfly” landing at Hainan Province, China. The recorded maximum wave height in this extreme climate event is over 10 m in the port. The economic losses and property damage due to the failure of offshore structures are huge each year around the world. Ocean engineers understand that an inappropriate design could result in instability of offshore structures, such as tilting or collapse in extreme climate events. They always pay their great attention on the dynamics of offshore structures under ocean wave and seismic wave loading (Ye, 2012c; Ye and Jeng, 2013). However, the dynamics of offshore structures and their seabed foundation under wave loading is still not fully understood; and analysis tools for ocean engineers involved in design are also limited. Therefore, the development of an effective, and reliable analysis tool for ocean engineers, and the investigation of the dynamics of offshore structures and their seabed foundation under wave loading is urgent and meaningful.

For the problem of interaction between ocean wave, offshore structure and its seabed foundation, there are three types of interaction mechanisms: fluid–structures interaction, wave–seabed interaction, and soil–structures interaction. Fluid–structures

\* Corresponding author.

E-mail address: [yejianhongcas@gmail.com](mailto:yejianhongcas@gmail.com) (J. Ye).

interaction is a relatively mature research topic in the computational fluid dynamics (CFD). Structures can be fixed, or flexible; as well as be impermeable or porous (Higuera et al., 2014a,b). However, the effect of seabed foundation is not taken into consideration in this mechanism. Soil–structures interaction was a traditional and classic topic in geotechnical engineering field in the past four decades. A great of effort has been made, and some valuable models are available currently to describe the interaction between seabed soil and offshore structures. In the early stage of investigation of FSSI problem, most researchers paid their attention on the wave–seabed interaction, ignoring the fluid–structures interaction and soil–structures interaction due to the limitation of analysis technology. The achievements include uncoupled analytical solution (Yamamoto et al., 1978; Hsu and Jeng, 1994; Tsai et al., 2000), coupled analytical solution (Lee et al., 2002; Lee and Lan, 2002) and uncoupled numerical model (Jeng et al., 2001), in which there was no a real offshore structure being considered. In these solutions and models, linear or nonlinear Stokes wave based on Laplace's equation was utilized to apply wave loading on seabed floor. Based on the above-mentioned research, some uncoupled numerical models considering the soil–structures interaction were further proposed (Mase et al., 1994; Ulker et al., 2009, 2012). However, wave loading on seabed floor was still based on Stokes wave; and the wave loading on marine structures is unknown. It is not difficult to see that the above-mentioned analytical solutions and uncoupled numerical models are insufficient to describe the interaction between ocean wave, offshore structure and its seabed foundation.

As an integrated system, coupled numerical model should be developed for wave–seabed–structures interaction. Mizutani et al. (1998, 1999) developed a BEM–FEM combined model for the problem of FSSI. However, their model cannot simulate complex wave motion, for example, wave breaking, and porous flow in seabed foundation and porous structures. Additionally, poro-elasto-plastic loose seabed soil cannot be dealt with by their model. Recently, Ye et al. (2013c) develop a more advanced coupled numerical model FSSI-CAS 2D for the problem of FSSI, in which RAVARN equation governing the fluid motion in fluid domain and porous flow in porous medium, dynamic Biot's equation governing the dynamics of marine structures and their seabed foundation. The reliability and suitability of FSSI-CAS 2D have been validated by an analytical solution, some laboratory wave flume tests and a centrifuge test (Ye et al., 2013c). FSSI-CAS 2D has been successfully applied to the FSSI problems in which regular wave (Jeng et al., 2013), breaking wave (Ye et al., 2014), and earthquake triggered tsunami wave (Ye et al., 2013b), poro-elasto-plastic loose seabed soil (Ye et al., 2015) are respectively involved. Under the same framework, FSSI-CAS 2D is further extended to three dimension, known as FSSI-CAS 3D. This 3D integrated numerical model for FSSI problem was validated using an analytical solution and a wave flume test (Ye et al., 2013a).

In real offshore environment, dense sediment and newly deposited loose sediment are both widely distributed. Under wave loading, they behave as elastic or elasto-plastic material, depending on the properties of seabed soil, such as relative density  $D_r$ , mean particles size  $d_{50}$ , and particles grading, and characteristics of wave loading, such as magnitude and loading rate. In this study, taking the developed three dimension integrated numerical model FSSI-CAS 3D as the analysis tool, the wave-induced dynamics of a caisson breakwater and its very dense elastic seabed foundation is investigated comprehensively. Actually, wave-induced scouring around offshore structures is also a common phenomenon in FSSI problem. However, visible wave-induced scouring occurring on seabed surface generally needs a long time, from hours to days, which is significantly longer than wave period. Therefore, scouring and dynamics of offshore structures and seabed foundation are the

physical problems with significantly different time scales. In previous investigations, these two physical problems generally were studied separately. Here, only the wave-induced dynamics of offshore structures and their seabed foundation is our focus. Consideration of wave-induced scouring of seabed in FSSI problem will be further conducted under the framework of CFD–DEM in the future. This study demonstrates that the advanced integrated numerical model for FSSI problem is a promising tool to evaluate the stability of offshore structures for ocean engineers in offshore industry.

## 2. 3D integrated numerical model for FSSI

### 2.1. Wave model

The wave motion on seabed, and its interaction with marine structures, as well as porous flow in seabed foundation are governed by using a modified Navier–Stokes equations. Sea water is treated as incompressible Newtonian fluid:

$$\nabla \cdot u_{fi} = 0 \quad (1)$$

$$\rho_f \left( \frac{\partial u_{fi}}{\partial t} + u_{fi} \frac{\partial u_{fi}}{\partial x_j} \right) = -\nabla p + \nabla \cdot \mu (\nabla u_{fi} + \nabla^T u_{fi}) + g_i + F_{si} + F_{di} \quad (2)$$

where  $u_{fi}$ ,  $u_{fj}$  ( $i, j = x, y, z$ ) represents the velocities of water,  $\rho_f$  is the density of water,  $p$  is the water pressure,  $g$  is the gravity, and  $F_{si}$  is the surface tension force, and  $\mu$  is the dynamic viscosity of sea water.  $F_{di}$  is the linear or nonlinear drag force between pore fluid and solid matrix in porous medium. In this integrated numerical model for FSSI, the above governing Eqs. (1) and (2) for wave motion and porous flow are solved by using a free N–S solver provided by the open source code TRUCHAS (2009) developed by US Los Alamos National Laboratory (LANL). In TRUCHAS, finite volume method (FVM) is adopted to solve the wave governing equations, and VOF method is adopted to trace the free surface of wave motion. The detailed physical algorithms can be found in the manual (Truchas, 2009). In the original source code of TRUCHAS, the Carman–Koseny relation proposed by Carman (1937) is adopted to formulate the linear drag force:

$$F_{di} = k \frac{(1-n)^2}{n^3} u_{fi} \quad (3)$$

where  $k$  and  $n$  are the permeability and porosity of porous medium, respectively. Obviously, the viscosity of fluid, mean particles diameter, and the effect of particles shape are all not taken into consideration in Eq. (3). According to Hur et al. (2010) and Hsu et al. (2002), the viscosity of fluid, mean particles diameter  $d_{50}$ , and shape of particles all have significant effect on the drag force between pore fluid and solid matrix. Therefore, the expression of drag force formulated in Eq. (3) is only a rough approximation. In this study, the drag force is formulated as

$$F_{di} = C_d \frac{\nu}{d_{50}^2} \frac{(1-n)^2}{n^2} u_{fi} \quad (4)$$

in which  $C_d$  is the laminar porous flow-induced drag force coefficient, and it is mainly related to the particles shape of solid matrix.  $\nu$  is the kinematic viscosity. In Eq. (4), the effect of the average diameter of particles in solid matrix, and the viscosity of pore water on the drag force are both considered.

It is noted here that Eq. (4) is also only applicable for linear laminar porous flow (Darcy's flow). As analyzed in Ye et al. (2013a), the exclusion of the nonlinear drag force in  $F_{di}$  would make a significant phase lag between the predicted response and the real response for wave-induced dynamics of marine structures. Meanwhile, there also would be a minor difference for peak

responses. As mentioned in Ye et al. (2013a), the inclusion of the nonlinear drag force in  $F_{di}$  will be developed in the future work.

In this 3D wave model, the internal wave maker proposed by Lin and Liu (1999) is applied to generate the target wave train, in which a mass function is added to the continuity Eq. (1) at the position where the wave maker is located. By applying different mass functions, various waves could be generated, for example, the linear wave, solitary wave, 2nd-order and 5th-order stokes wave, conoidal wave, etc.

### 2.2. Soil model

It has been commonly known that soil is a multi-phase material consisting of soil particles, water and trapped air. In the soil mixture, the soil particles form the skeleton; the water and the air fill the void of skeleton. Therefore, soil is a three-phase porous material, rather than a continuous medium. In this study, the dynamic Biot's equation known as “ $u-p$ ” approximation proposed by Zienkiewicz et al. (1980) is used to govern the dynamic response of the porous response under wave loading, in which the relative displacements of pore fluid to soil particles are ignored, but the acceleration of the pore water and soil particles is included:

$$\frac{\partial \sigma_x}{\partial x} + \frac{\partial \tau_{xy}}{\partial y} + \frac{\partial \tau_{xz}}{\partial z} = -\frac{\partial p_s}{\partial x} + \rho \frac{\partial^2 u_s}{\partial t^2}, \quad (5)$$

$$\frac{\partial \tau_{xy}}{\partial x} + \frac{\partial \sigma_y}{\partial y} + \frac{\partial \tau_{yz}}{\partial z} = -\frac{\partial p_s}{\partial y} + \rho \frac{\partial^2 v_s}{\partial t^2}, \quad (6)$$

$$\frac{\partial \tau_{xz}}{\partial x} + \frac{\partial \tau_{yz}}{\partial y} + \frac{\partial \sigma_z}{\partial z} + \rho g = -\frac{\partial p_s}{\partial z} + \rho \frac{\partial^2 w_s}{\partial t^2}, \quad (7)$$

$$k \nabla^2 p_s - \gamma_w n \beta \frac{\partial p_s}{\partial t} + k \rho_f \frac{\partial^2 \epsilon_v}{\partial t^2} = \gamma_w \frac{\partial \epsilon_v}{\partial t}, \quad (8)$$

where  $(u_s, v_s, w_s)$  are soil displacements in the  $x$ -,  $y$ - and  $z$ -directions, respectively;  $n$  is the soil porosity;  $\sigma_x, \sigma_y$  and  $\sigma_z$  are effective normal stresses in the horizontal and vertical directions;  $\tau_{ij}(i, j = x, y, z)$  is the shear stress;  $p_s$  is the pore water pressure;  $\rho = \rho_f n + \rho_s(1-n)$  is the average density of porous seabed;  $\rho_f$  is the fluid density;  $\rho_s$  is the solid density;  $k$  is Darcy's permeability;  $g$  is the gravitational acceleration,  $\gamma_w$  is the unit weight of water, and  $\epsilon_v$  is the volumetric strain of soil. In Eq. (8), the compressibility of pore fluid ( $\beta$ ) and the volume strain ( $\epsilon_v$ ) are defined as

$$\beta = \left( \frac{1}{K_f} + \frac{1-S_r}{p_{w0}} \right), \quad (9)$$

$$\epsilon_v = \frac{\partial u_s}{\partial x} + \frac{\partial v_s}{\partial y} + \frac{\partial w_s}{\partial z}, \quad (10)$$

where  $S_r$  is the degree of saturation of seabed,  $p_{w0}$  is the absolute static pressure and  $K_f$  is the bulk modulus of pore water ( $K_f = 2.24 \times 10^9 \text{ N/m}^2$ ).

In the above governing equations, the effective stresses can be determined applying Hooke's law for elastic seabed foundation:

$$\sigma'_{ij} = D_{ijkl} \epsilon_{kl}, \quad (11)$$

where  $\sigma'_{ij}$  is effective stresses in seabed soil,  $\epsilon_{kl}$  is the strain of soil.  $D_{ijkl} = 2G(\delta_{ik}\delta_{jl} + \frac{\nu}{1-2\nu}\delta_{ij}\delta_{kl})$ ,  $G$  and  $\nu$  are the elastic shear modulus and Poisson's ratio, respectively.

Finite element method (FEM) is used to solve the above governing Eqs. (5)–(8). The discretized forms of the above governing Eqs. (5)–(8) are

$$M\ddot{\mathbf{u}} + K\mathbf{u} - Q\mathbf{p} = f^{(1)}, \quad (12)$$

$$G'\ddot{\mathbf{u}} + Q^T\ddot{\mathbf{u}} + S\mathbf{p} + H\mathbf{p} = f^{(2)}, \quad (13)$$

where  $\mathbf{u}$  and  $\mathbf{p}$  are the nodal displacements and the pore pressure vectors respectively.  $M, K, Q, G', S,$  and  $H$  are the mass, stiffness, coupling, dynamic seepage force, compressibility, and permeability matrixes, respectively. The Generalized Newmark  $p$ th order scheme for  $j$ th order equation scheme is adopted to calculate time integration when solving the above discretized matrix equations. The definition of coefficient matrixes  $M, K, Q, G', S, H, f^{(1)}, f^{(2)}$ , and the detailed information of the 3D numerical method to solve the dynamic Biot's equations can be found in Ye (2012b).

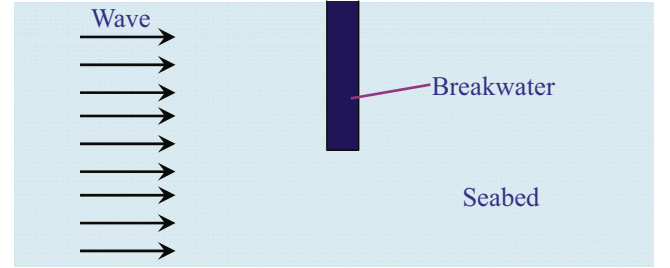


Fig. 1. Top-view of the breakwater, seabed and ocean wave system in the computational domain.

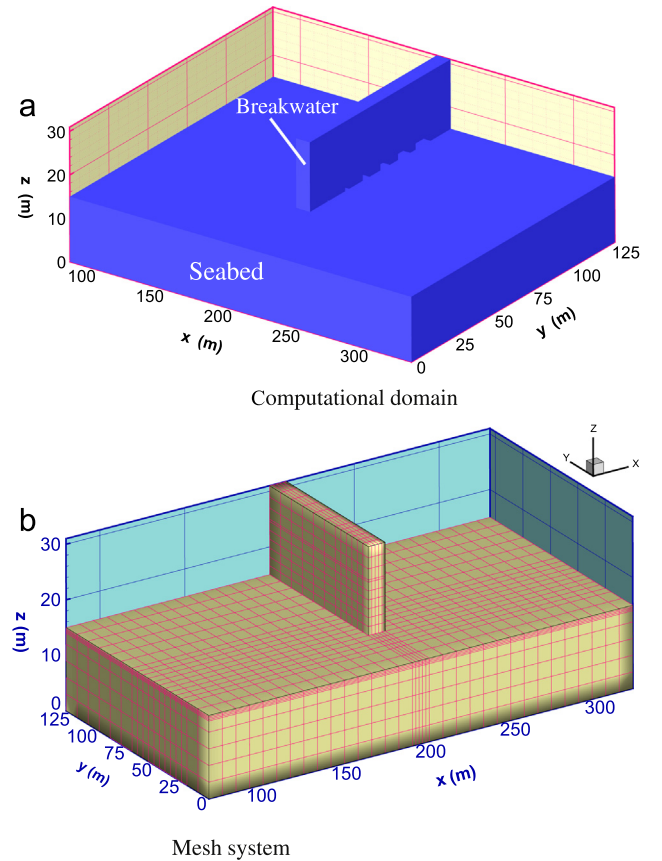


Fig. 2. The chosen computational model: 3D seabed foundation and caisson breakwater system.

Table 1 Properties of the seabed foundation and caisson breakwater used in computation.

Medium	$E$ (Pa)	$\nu$	$k$ (m/s)	$S_r$ (%)	$n$	$G_s$
Seabed	$2.0 \times 10^7$	0.3333	$1.0 \times 10^{-5}$	98	0.25	2.65
Caisson breakwater	$1.0 \times 10^{10}$	0.25	0.0	0.0	0.1	2.65

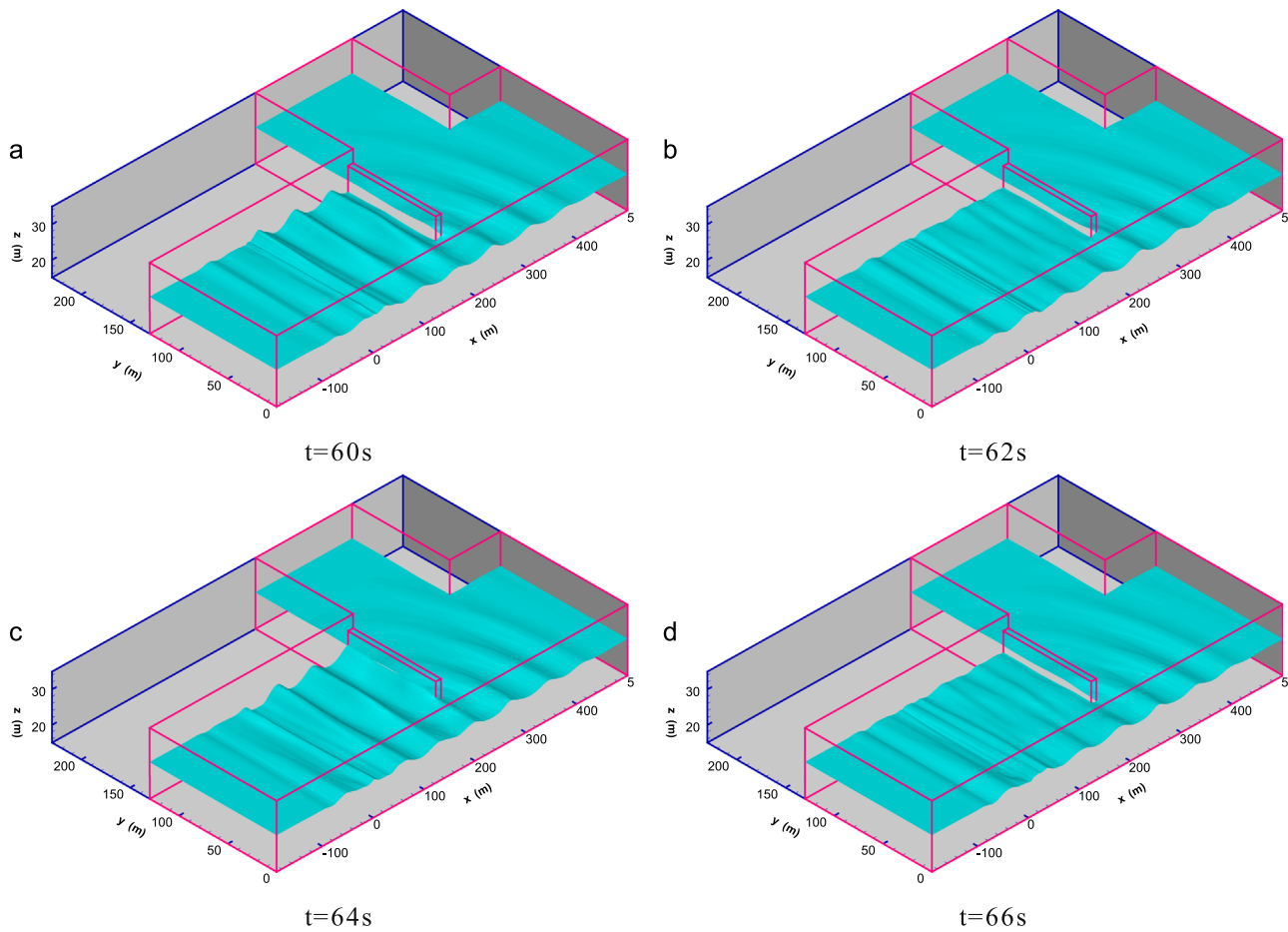


Fig. 3. Wave profile around the caisson breakwater at typical times  $t=60$  s, 62 s, 64 s and 66 s.

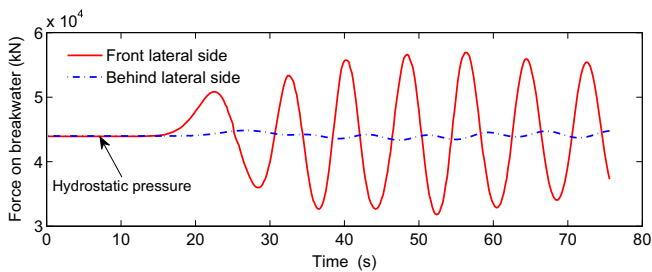


Fig. 4. Total wave impact force acting on the front and behind lateral sides of caisson breakwater (hydrostatic plus wave-induced pressure).

### 2.3. Integration and verification

In this integrated numerical model, the non-match mesh scheme and non-match time step are used in coupling computation. A data exchange port is developed adopting 3D Shepard interpolation method to transmit data at the interface between fluid domain and solid domain. In the integrated model, the pressure continuity on interfaces between fluid domain and solid domain is applied in computation. The wave model is responsible for the generation, propagation of wave, and determines the pressure acting on seabed and marine structures. At the meantime, the pressure/force acting on seabed and marine structures determined by the wave model is transmitted to the soil model through the developed data exchange port. Taking the pressure/force acting on seabed and marine structures as the boundary value, the dynamic response of seabed and marine structures is

determined by the soil model. More information about this integrated model can be found in Ye (2012b) and Ye et al. (2013a).

It seems that a one way coupling is used in computation. There is no feedback from solid domain to fluid domain. Actually, the coupling between the wave model and soil model can be referred as a semi-coupling process (Ye et al., 2013c), because the seabed foundation and rubble mound are considered as porous medium in the wave model when determining the wave field; the effect of porosity of seabed foundation and rubble mound on wave field has been taken into consideration. Therefore, the flow field in fluid domain and solid domain is continuous at their interfaces. However, the displacement at interfaces is not continuous. From the point view of physics, the wave-induced vibration of marine structures and seabed foundation generally is apparently minor comparing with the wave length. The discontinuity of displacement between fluid domain and solid domain is acceptable. If displacement continuity on interfaces must be implemented through iterative process (fully coupled), the computation will be very expressive. Additionally, as far as we know, there is no code so far that can implement the fully coupled computation for wave–seabed–structures interaction model.

The developed integrated numerical model for FSSI has been validated by an analytical solution proposed by Hsu and Jeng (1994), and by a wave flume test involving submerged rubble mound breakwater conducted by Mizutani et al. (1998). The detail information on verification work can be found in Ye et al. (2013a). The verification work shows that the integrated numerical model is applicable for problem of fluid–structures–seabed interaction.

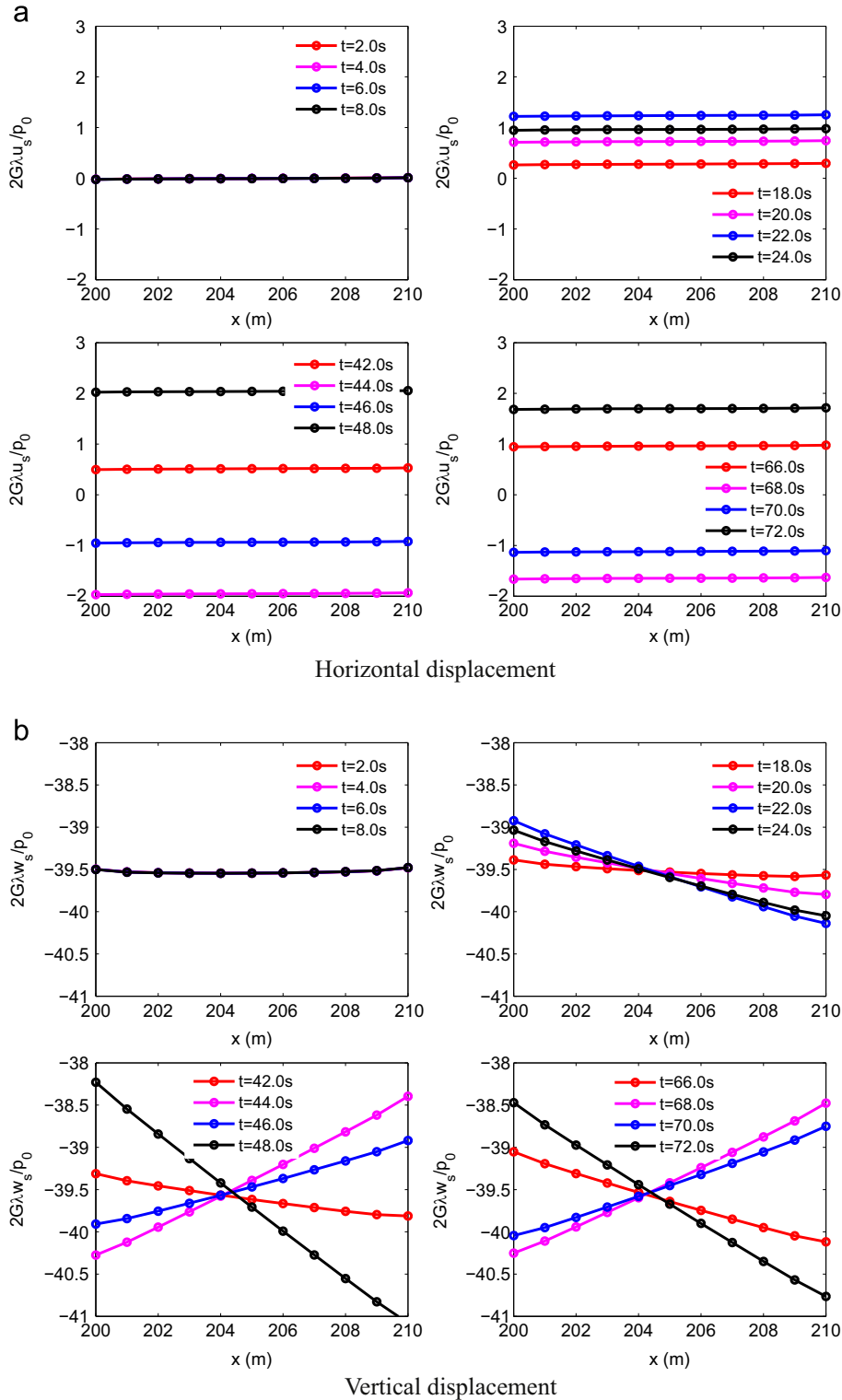


Fig. 5. Motion of the bottom of caisson breakwater under the nonlinear wave loading. ( $G$  is the shear modulus,  $\lambda$  is the wave number,  $p_0 = \frac{\gamma_w d}{2 \cosh(\lambda d)}$ ,  $d$  is the depth of seawater).

### 3. Computational domain and boundary condition

Fig. 1 shows the top-view of a breakwater, seabed and ocean wave system involved in the study. A caisson breakwater is built on an elastic seabed (very dense sand bed). A 3D ocean wave normally propagates to the caisson breakwater from seaward side to onshore side. Fig. 2(a) is the chosen computational domain for the breakwater, seabed and ocean wave system. The dimension of

seabed foundation is  $L_x=250$  m (length),  $L_y=130$  m (width) and  $h=15$  m (thickness). The breakwater is 90 m long, 10 m wide and 16 m high. Its coordinate range built on the elastic seabed is  $x=200-210$  m,  $y=40-130$  m,  $z=15-31$  m. The 27-nodes hexahedral iso-parametric elements are used to discretize the seabed foundation and the caisson breakwater (Fig. 2(b)). Due to the fact that 27-nodes iso-parametric element own complete third-order accuracy, the computational errors could be controlled effectively;

and the size of elements could be significantly larger than that if 8-nodes elements (only first-order accuracy) are used. Totally, 6000 elements, 100,000 nodes are generated in the breakwater and its seabed foundation. The time step is set as  $T/40$  in dynamic analysis, where  $T$  is the wave period.

In numerical computation, the following boundary conditions are applied according to the actual engineering environment of the breakwater located.

First, the bottom of the elastic seabed foundation is rigid as rigid and impermeable:

$$u_s = v_s = w_s = 0 \quad \text{at} \quad z = 0 \quad (14)$$

Second, the four lateral sides of seabed foundation are fixed in the  $x$  direction or in the  $y$  direction:  $\ni$

$$u_s = 0 \quad \text{at} \quad x = 80 \text{ m} \quad \text{and} \quad x = 330 \text{ m} \quad (15)$$

$$v_s = 0 \quad \text{at} \quad y = 0 \text{ m} \quad \text{and} \quad y = 130 \text{ m} \quad (16)$$

Third, on the surface of seabed foundation (except the part beneath the caisson breakwater), the pore pressure is equal to the combination of wave-induced pressure and the hydrostatic water pressure (pore pressure continuity on interfaces).

Fourth, on the surface of the caisson breakwater (except the bottom), the pore pressure is zero due to the fact that the caisson is impermeable. However, the breakwater is still applied by the wave-induced pressure and the hydrostatic water pressure on its lateral surfaces.

Fifth, due to the fact that the caisson breakwater is impermeable, it is applied by a floating force on its bottom. This floating force on bottom of caisson is necessary to be considered. Otherwise, the

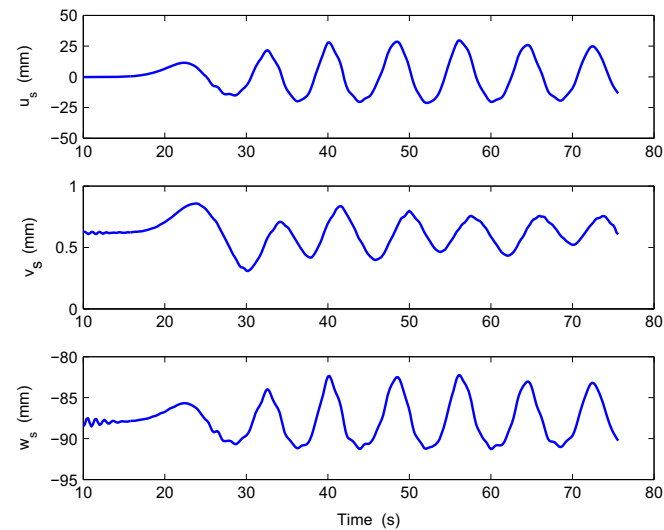


Fig. 6. Displacements of the top-left corner ( $x=200$  m,  $y=80$  m,  $z=31$  m) of caisson breakwater under the nonlinear wave loading.

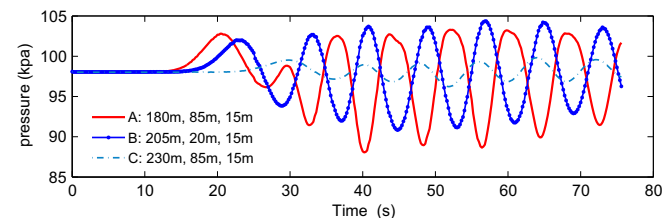


Fig. 7. Nonlinear wave-induced water pressure acting on seabed surface at different locations around the caisson breakwater.

effective stresses in the seabed foundation, settlement of the caisson breakwater will be significantly overestimated (Ye et al., 2012).

#### 4. Dynamic response of caisson breakwater

The seabed generally has experienced the consolidation process under hydrostatic pressure and self-gravity in the geological history. There is no excess pore pressure in the seabed foundation. This consolidation status should be first determined, and taken as the initial condition for the thereafter wave-induced dynamic analysis for the caisson breakwater and seabed foundation system. Here, the properties of seabed foundation and caisson breakwater used in computation are listed in Table 1. The detail information about the consolidation of 3D seabed foundation under a caisson breakwater can be found in Ye et al. (2012).

Under the environmental loading (ocean wave), breakwater built on an elastic seabed would lose its stability due to excess shear stress and liquefaction of seabed foundation. The dynamic response of breakwater and its seabed foundation is the main concern of coastal engineers involved in design. Taking the above determined consolidation status as the initial condition, the dynamic response of caisson breakwater and its seabed foundation under 3D wave loading is analyzed.

3D ocean wave field propagating on elastic seabed around the caisson breakwater is first determined by utilizing the 3D wave model in each time step. The wave characteristics for the 3D wave maker is: wave height  $H=1.5$  m, water depth  $d=10$  m, and wave period  $T=8.0$  s. In the computational domain of the 3D ocean wave, three absorb zones are set to eliminate the unexpected reflected wave due to limited computational domain. The three absorb zones are allocated at: Zone one ( $x=-190$  m to  $-100$  m,  $y=0-130$  m), Zone two ( $x=400-500$  m,  $y=0-130$  m), Zone three: ( $x=210-400$  m,  $y=130-230$  m). The wave maker is located at the position  $x=0$  m. The number of mesh for the 3D wave simulation is up to 3 millions. Parallel computation in TRUCHAS is utilized in simulation.

Fig. 3 shows the wave profile around the caisson breakwater at four typical times (in one wave period). It can be seen that there are three wave zones: standing wave in front of the caisson breakwater, diffracted wave behind the caisson breakwater, and progressive wave near to the head of breakwater. The standing wave is formed due to the interference between incident wave and reflected wave in front of the breakwater; the wave height of this standing wave is

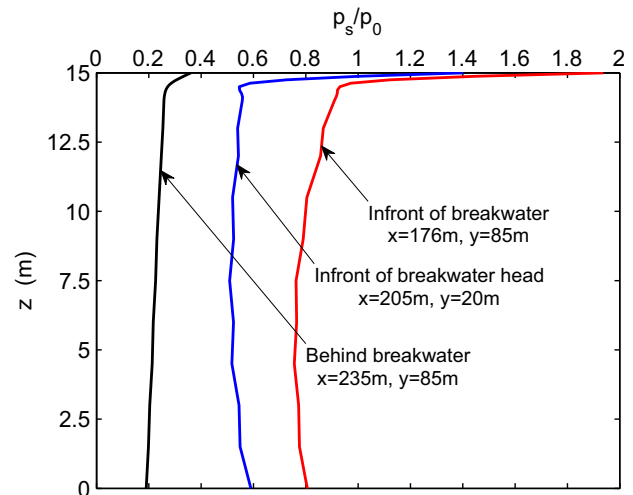


Fig. 8. Distribution of the nonlinear wave-induced maximum dynamic pressure in seabed foundation at three typical locations.  $p_0$  is the pressure induced by linear wave  $p_0 = \gamma_w H / 2 \cosh(\lambda d)$ , where  $\lambda$  is the wave number.

about 3.0 m, two times of the original height of incident wave. The diffracted wave behind the caisson breakwater is formed due to the block effect of the breakwater to incident wave.

Wave impact force on the lateral sides of caisson breakwater is the main driven force to make the breakwater vibrate. Fig. 4 illustrates the wave impact force acting on the front and behind lateral sides of the caisson breakwater. It can be seen that the wave impact force on the front lateral side of breakwater is significantly much larger than that on the behind lateral side of breakwater. Therefore, the standing wave in front of caisson breakwater should be the dominant factor for shear failure and liquefaction of seabed foundation.

The vibration characteristic of the breakwater under wave loading is illustrated in Fig. 5. Before the wave arriving at the breakwater, it keeps its initial static status. After the wave arriving, the breakwater

begins to move forward and backward on horizontal direction, and swings on vertical direction periodically. As a whole, the breakwater moves and swings to right hand side when wave crests arrive; and it moves and swings to left hand side when wave troughs arrive. Fig. 6 demonstrates the displacements of the top-left corner of the caisson breakwater. It is shown that the maximum horizontal displacement at the top-left corner is greater than 30 mm.

### 5. Dynamic response of seabed foundation

The wave-induced dynamic response of the seabed foundation around the caisson breakwater is particularly important for the stability of the caisson breakwater due to the fact that liquefaction,

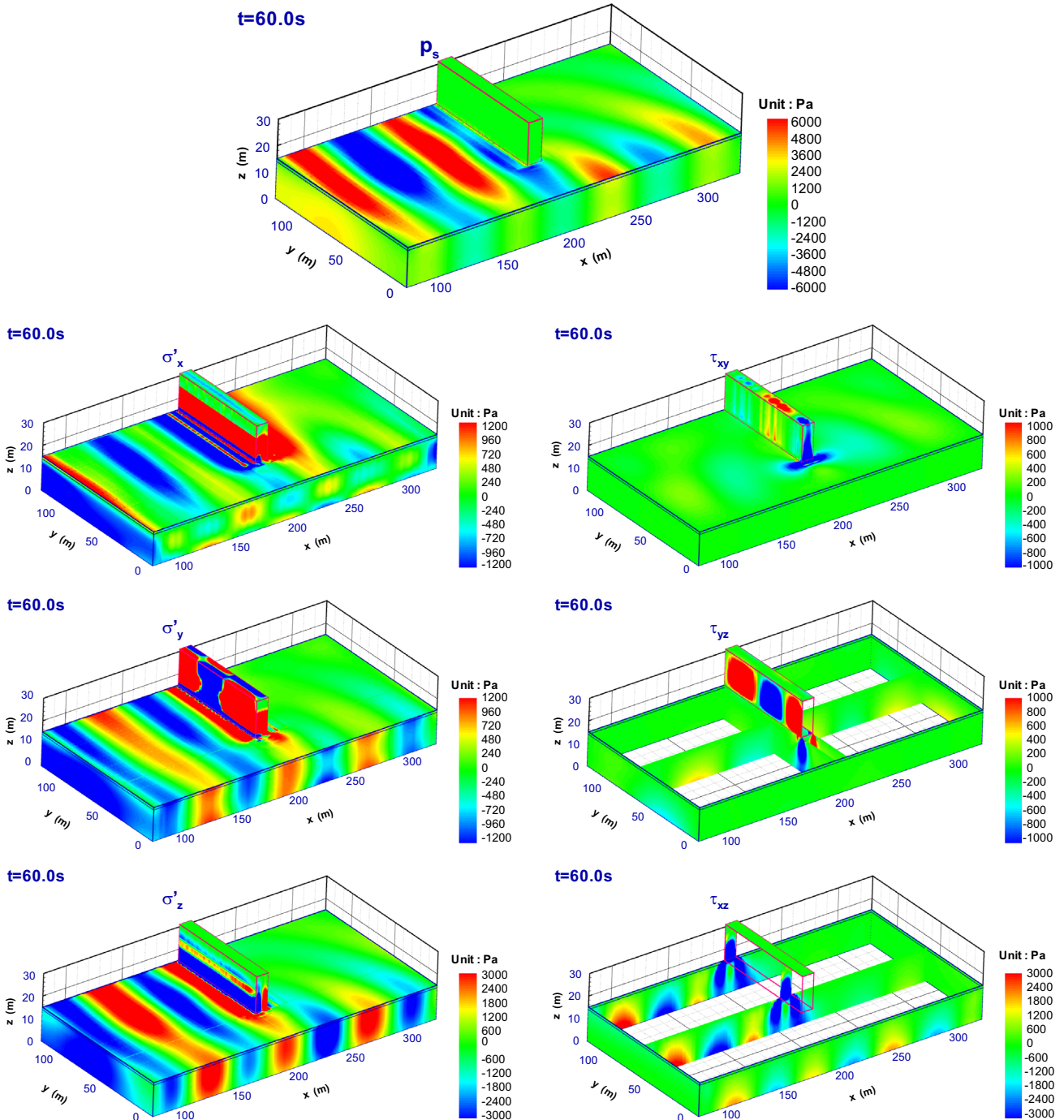


Fig. 9. Wave-induced dynamic response in the seabed foundation at time  $t=60$  s.

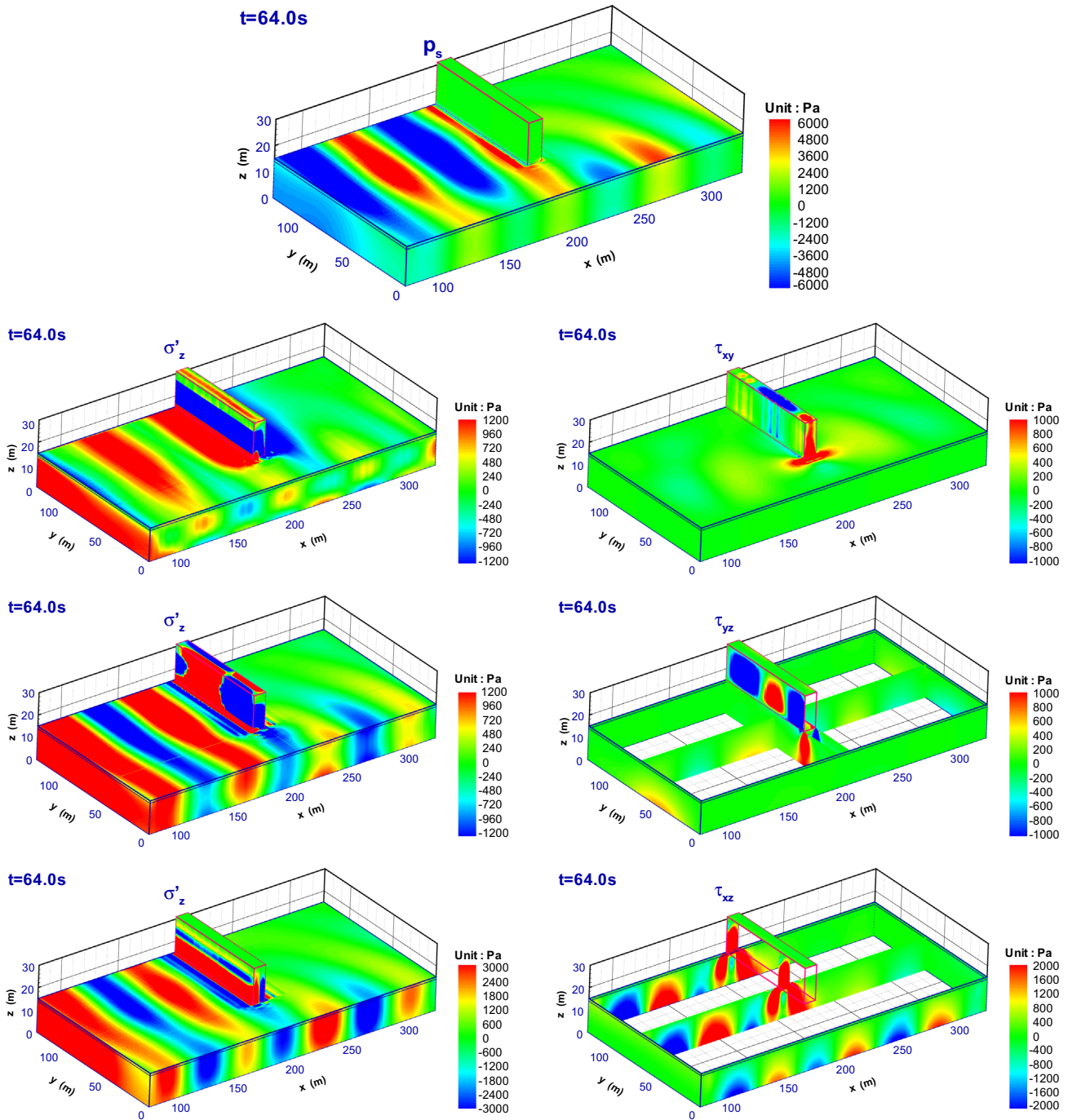


Fig. 10. Wave-induced dynamic response in the seabed foundation at time  $t=64$  s.

and shear failure could probably occur. In this section, the wave-induced dynamic response, and shear failure are investigated.

As mentioned in the above section, there are three kinds of wave fields around the caisson breakwater. Correspondingly, the wave-induced dynamic pressure acting on different parts of the seabed around the breakwater is significantly different. Fig. 7 illustrates the wave-induced water pressure acting on the seabed surface at three typical positions A ( $x=180$  m,  $y=85$  m,  $z=15$  m, in front of the breakwater), B ( $x=230$  m,  $y=85$  m,  $z=15$  m, behind the breakwater), and C ( $x=205$  m,  $y=20$  m,  $z=15$  m, near to the breakwater head). It can be seen that the standing wave-induced pressure in front of the breakwater is greatest; and the non-linearity is strong. The diffracted wave-induced pressure behind

the breakwater is smallest. It is indicated that the breakwater indeed can effectively protect the seabed behind it.

The wave-induced pressure acting on the seabed around the breakwater is significantly different. It results in that the wave-induced seabed response is correspondingly different. Fig. 8 demonstrates the vertical distribution of the wave-induced maximum pore pressure in the seabed foundation at the three typical positions. It can also be seen that the standing wave-induced maximum pore pressure in front of the breakwater is greatest, while the diffracted wave-induced pore pressure behind the breakwater is smallest. The progressive wave-induced pore pressure near to the breakwater head is between those. It indicates that the wave-induced momentary liquefaction is most likely to occur in front of the caisson breakwater.

Figs. 9 and 10 demonstrate the distribution of wave-induced dynamic response in the seabed foundation at two typical times  $t=60$  s (wave trough arriving) and  $t=64$  s (wave crest arriving). It can be further clearly observed that the seabed response in front of the caisson breakwater is much stronger than that behind the caisson breakwater. It is also further indicated that the breakwater can effectively block the wave energy coming from seaward side, and protect the seabed foundation behind it. Another phenomenon observed is that the wave-induced pore pressure in the seabed foundation is positive, dynamic  $\sigma'_z$  and  $\sigma'_y$  is compressive, and dynamic  $\sigma'_x$  is tensile under wave crest. Oppositely, the wave-induced pore pressure is negative, dynamic  $\sigma'_z$  and  $\sigma'_y$  is tensile, and dynamic  $\sigma'_x$  is compressive under wave trough. According to the liquefaction criterion proposed by Okusa (1985), if the wave-induced tensile dynamic  $\sigma'_z$  is great enough to overcome the overburdened weight of soil, the seabed foundation will liquefy transiently. Based on this criterion, the seabed foundation will not liquefy under wave crest. At time  $t=60$  s, a wave trough arrives at the breakwater, the wave-induced pore pressure is negative, and the dynamic  $\sigma'_z$  is tensile in the zone close to the bottom of the breakwater, where it is highly possible for the seabed foundation to transiently liquefy. At time  $t=64$  s, a wave crest arrives at the breakwater, the seabed foundation close to the bottom of the breakwater is unlikely to liquefy. However, the strong pushing wave impact force would overthrow the breakwater. Therefore, the liquefaction of seabed foundation and tilting of the breakwater both should be taken into consideration in structural design. The liquefaction characteristics of the seabed foundation under wave loading will be intensively investigated in the next section.

Wave-induced shear stresses  $\tau_{xy}$  and  $\tau_{yz}$  are only concentrated in the region under the caisson breakwater head. Their magnitude reaches up to 2 kPa. In the other region far away from the breakwater, the wave-induced  $\tau_{xy}$  and  $\tau_{yz}$  are relatively small, only up to about 500 Pa. Wave-induced  $\tau_{xy}$  and  $\tau_{yz}$  in the seabed foundation is the secondary factor for the stability of breakwater. While wave-induced  $\tau_{xz}$  generally is the dominant factor for the shear failure of seabed foundation. Wave-induced  $\tau_{xz}$  in the region far away from the breakwater is distributed in the lower part of seabed foundation. Its magnitude can reach up to 3 kPa. However, the shear failure would not occur in the lower part of seabed foundation. It is observed that wave-induced  $\tau_{xz}$  is highly concentrated in the zone under the caisson breakwater. The maximum magnitude could reach up to 10 kPa. Under the periodical wave loading, the direction of dynamic  $\tau_{xz}$  changes from the right to the left periodically. This wave-induced cyclic dynamic shear stress is a very dangerous factor for the stability of the breakwater. Fig. 12(a) shows the time history of  $\tau_{xz}$  in the process wave loading at two typical positions. Before the wave arriving,  $\tau_{xz}$  is determined in the consolidation status. After the wave arriving, wave-induced  $\tau_{xz}$  varies periodically.

Mohr–Coulomb criterion is generally adopted to judge the occurrence of shear failure in the granular materials. The stress angle  $\theta_{MC}$  is frequently taken as the representative physical quantity (Fig. 11). The shear failure criterion is expressed as:

$$\theta_{MC} = \arctan \left\{ \frac{\frac{\sigma'_1 - \sigma'_3}{2}}{\frac{c}{\tan \phi} + \frac{\sigma'_1 + \sigma'_3}{2}} \right\} = \phi \quad (17)$$

where  $\theta_{MC}$  is the stress angle,  $c$  and  $\phi$  are the cohesion and the internal friction angle of soil, respectively.  $\sigma'_1$  and  $\sigma'_3$  are the maximum and minimum principle stresses, respectively.

Fig. 12(b) illustrates the variation of stress angle at the same positions involved in Fig. 12(a). It is observed that the stress angles are both  $28.6^\circ$  in consolidation status. After wave arriving, the stress angle at the two positions varies periodically. The variation magnitude is about  $1.5^\circ$  at  $(x=201 \text{ m}, y=85 \text{ m}, z=14 \text{ m})$ , and

about  $2.0^\circ$  at  $(x=209 \text{ m}, y=85 \text{ m}, z=14 \text{ m})$ . Furthermore, the variation regulation of the stress angle at the two positions is completely opposite. This phenomenon can be attributed to the symmetry of the two positions along  $x=205 \text{ m}$ . Generally, the internal friction angle of sandy seabed foundation is  $28^\circ\text{--}35^\circ$ . Therefore, the shear failure is possible to occur in the zone under the caisson breakwater depending on the wave characteristics and seabed soil property. In the practice of engineering, the replacement of the sandy seabed using gravel materials under marine structures is a suggested method to avoid the occurrence of wave-induced shear failure.

### 6. Momentary liquefaction in seabed foundation

It is well known that very dense seabed and loose seabed would both exist in offshore environment. The newly deposited loose sand bed is a typical seabed, which responds to cyclic loading with unrecoverable deformation. The bearing capacity of a loose seabed is also weak. Under dynamic loading, such as ocean wave and seismic wave, soil compaction due to the rearrangement of soil particles occurs, making the arrangement

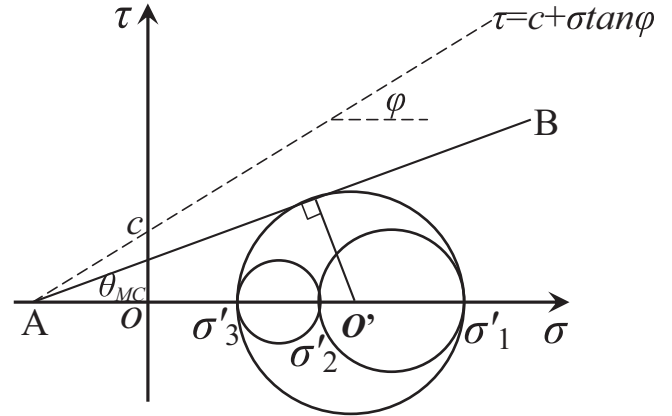


Fig. 11. Mohr–Coulomb criterion for the shear failure in granular materials.

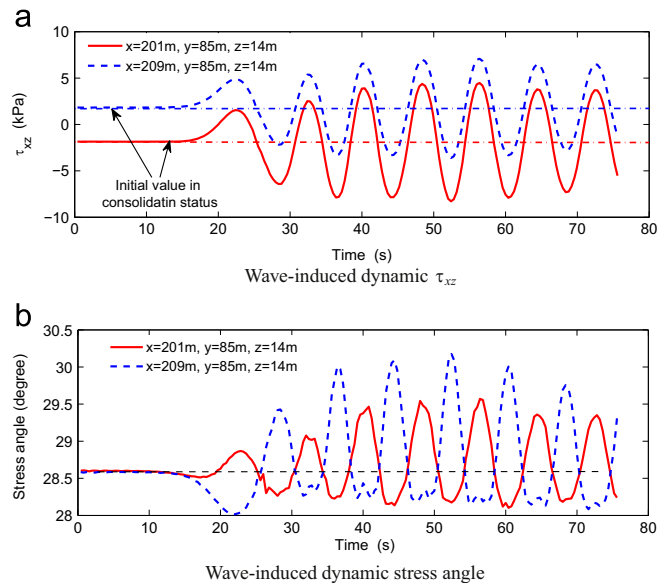
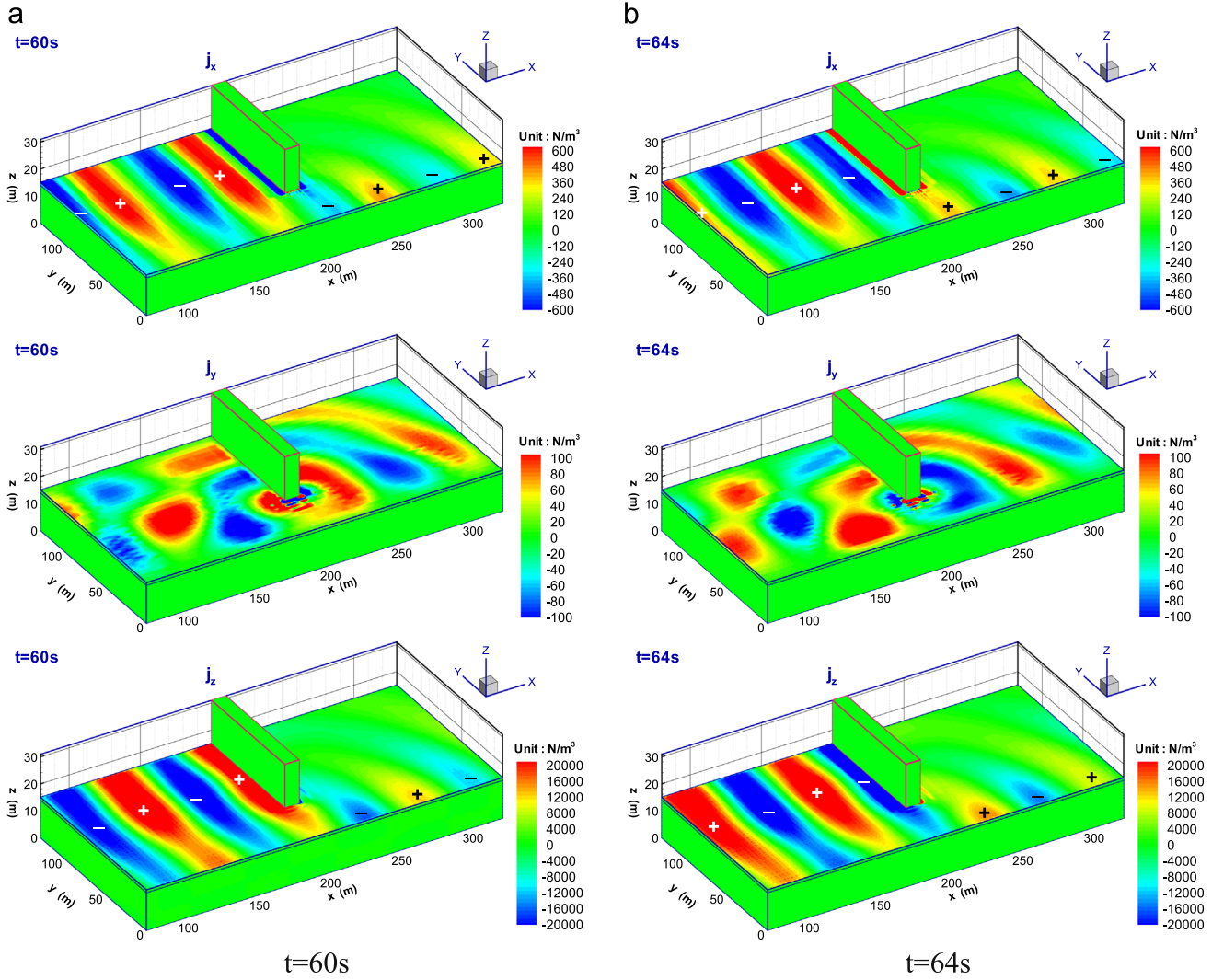


Fig. 12. Historic curve of shear stress  $\tau_{xz}$  and corresponding stress angle under the 3D wave loading at two typical positions ( $x=201 \text{ m}, y=85 \text{ m}, z=14 \text{ m}$ ) and ( $x=209 \text{ m}, y=85 \text{ m}, z=14 \text{ m}$ ), which are both under the caisson breakwater.



**Fig. 13.** Distribution of the wave-induced seepage force  $j_x$ ,  $j_y$  and  $j_z$  at two typical times  $t=60$  s and  $t=64$  s. The positive seepage force is upward; and the negative seepage is downward.

of these soil particles gradually tend to reach to an optimal state accompanying several residual liquefaction (DeGroot et al., 2006; Kudella et al., 2006; Kirca et al., 2013) and reconsolidation processes (Miyamoto et al., 2004). After long-term dynamic loading in geological history, the soil particles in a loose seabed could contact with each other very densely. Finally, the soil compaction due to the plastic volumetric deformation is unlikely to occur again under dynamic loading. A loose seabed becomes a very dense elastic seabed. Nowadays, dense seabed sporadically exists in offshore environment. In the practice of engineering, coastal engineers generally always manage to choose a very dense seabed as the seabed foundation of marine structures due to its strong bearing capacity, and only momentary liquefaction could occur in them. Evaluation of wave-induced momentary liquefaction in very dense seabed foundation of offshore structures is meaningful for the purpose of structures stability.

The wave-induced momentary liquefaction in an elastic dense seabed foundation would be one of the main reasons for the instability of breakwater in offshore environments. The liquefaction characteristics of seabed foundation under 3D wave loading should be paid special attention by coastal engineers in structures design. In this study, the momentary liquefaction in dense seabed around the caisson breakwater is investigated. The wave-induced

residual liquefaction in a loosely deposited seabed foundation at 3D scale will be further investigated in the future.

Okusa (1985) proposed a 1D liquefaction criterion based on the initial and wave-induced vertical effective stresses  $\sigma'_{z0}$  and  $\sigma'_{zd}$ :

$$\sigma'_{zd} \geq -\sigma'_{z0} \quad (18)$$

In the above liquefaction criterion,  $\sigma'_{z0}$  is considered as the prevention of liquefaction; and  $\sigma'_{zd}$  is the wave-induced dynamic vertical effective stress. It is the driven force for liquefaction. However, the effect of initial horizontal effective stresses  $\sigma'_{x0}$  and  $\sigma'_{y0}$  on preventing the liquefaction has not been considered. Tsai (1995) further extended the above 1D liquefaction criterion to 3D condition:

$$\frac{1}{3}(\sigma'_{x0} + \sigma'_{y0} + \sigma'_{z0}) + \frac{1}{3}(\sigma'_{xd} + \sigma'_{yd} + \sigma'_{zd}) \geq 0 \quad (19)$$

$\sigma'_{xd}$  and  $\sigma'_{yd}$  are the wave-induced dynamic horizontal effective stresses. This liquefaction criterion only adopts the average idea. There is no clear physical meaning of how the  $\sigma'_x$  and  $\sigma'_y$  affect the liquefaction potential of soil. Recently, Ye (2012a) proposed another 3D liquefaction criterion to consider the effect of cohesion and internal friction angle of soil:

$$\sigma'_z + 2(c - \sigma'_x \tan \phi)u(-\sigma'_x) + 2(c - \sigma'_y \tan \phi)u(-\sigma'_y) \geq 0 \quad (20)$$

in which  $u(x)$  is the unit step function.  $c$  and  $\phi$  are the cohesion and the internal friction of soil, respectively.  $\sigma'_x$ ,  $\sigma'_y$  and  $\sigma'_z$  are the

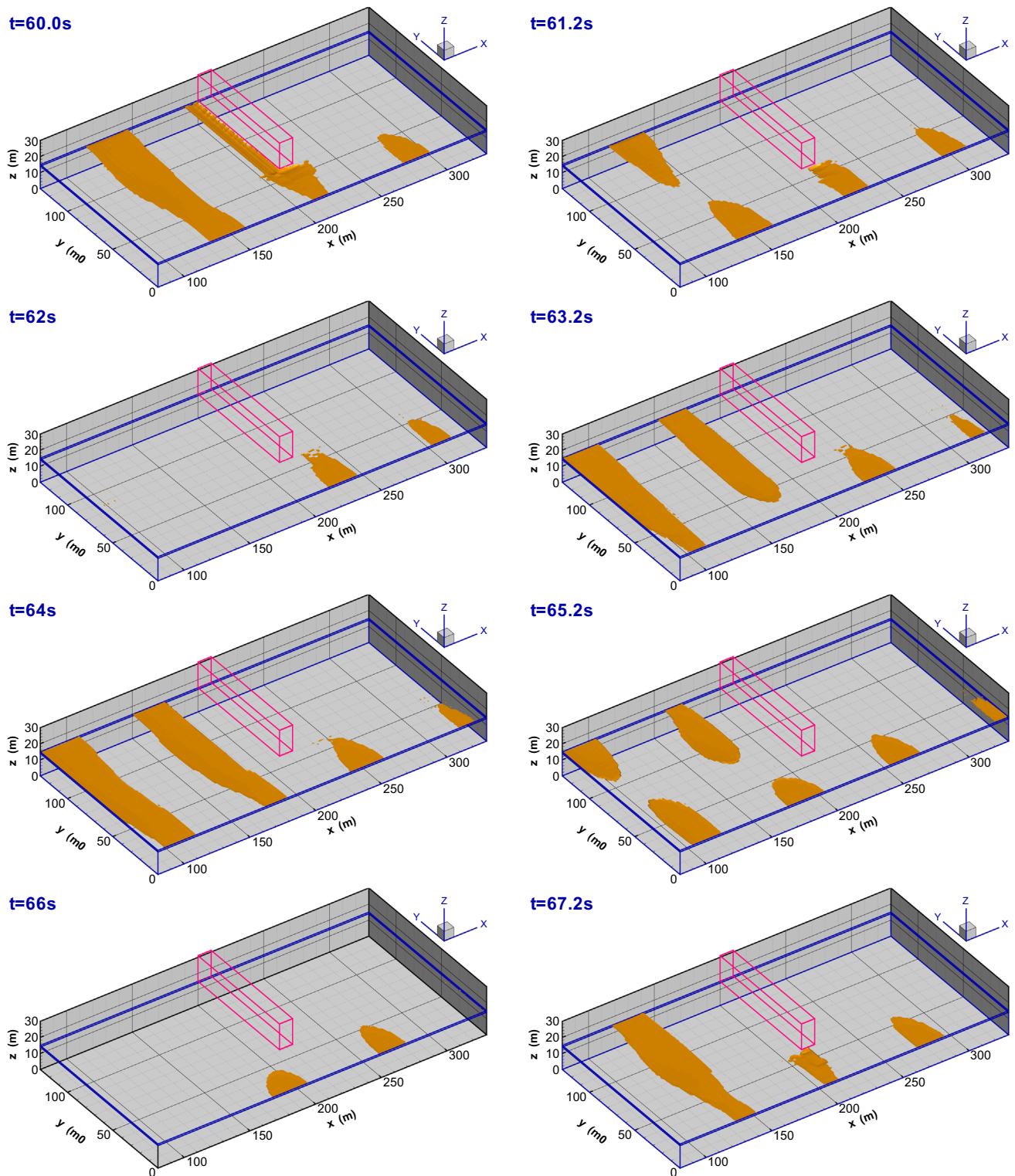


**Fig. 14.** Predicted momentary liquefaction zone near the seabed surface under the 3D wave loading in a typical wave period from  $t=60$  s to  $t=68$  s. The liquefaction criterion proposed by Ye (2012a) is used.

current effective stress states. For sandy soil, the cohesion  $c$  normally is 0. Ye (2012a) claims that the 3D liquefaction criterion proposed by Tsai (1995) is a special form of the liquefaction criterion considering the cohesion and friction angle when  $c=0$  and  $\phi=26.6^\circ$ . In this study, the 3D liquefaction proposed by Ye (2012a) is used.

The essence of momentary liquefaction in the seabed foundation under wave loading is that wave-induced upward seepage

force overcomes the overburdened weight of soil, making the contact effective stresses between soil particles become zero. As pointed out in Ye (2012b), the upward seepage force only exists in the zones under wave troughs; the seepage force in the zones under wave crests is downward. The seabed under wave trough could liquefy transiently if the upward seepage force is sufficient to overcome the overburdened weight of soil and structures; however, the seabed under wave crest is impossible to liquefy.

Therefore, the momentary liquefaction in the seabed foundation is mainly dependent on the magnitude of seepage force, and its direction. The three components of seepage force in the seabed foundation are expressed as:

$$j_x = \frac{\partial p_s}{\partial x}, \quad j_y = \frac{\partial p_s}{\partial y}, \quad j_z = \frac{\partial p_s}{\partial z} \quad (21)$$

Fig. 13 illustrates the distribution of wave-induced seepage force  $j_x$ ,  $j_y$  and  $j_z$  at two typical times  $t=60$  s and  $t=64$  s. It can be seen that the distribution form of the wave-induced seepage force  $j_x$ ,  $j_y$  and  $j_z$  at time  $t=60$  s and  $t=64$  s is basically the same. However, their direction of these seepage forces is completely opposite at the two times. That is because the time interval between the two times is 4 s, which is exactly half of the wave period. The wave crest and the wave trough on the seabed at time  $t=60$  s become wave trough, and wave crest on the same seabed at time  $t=64$  s. It is also clearly found that the wave-induced seepage force  $j_x$ ,  $j_z$  in front of the caisson breakwater is much greater than that behind the caisson breakwater. This phenomenon indicates that the protection of the breakwater for the seabed behind it is effective. Comparing with the vertical seepage force  $j_z$ , the horizontal seepage force  $j_x$  and  $j_y$  is very small. The maximum magnitude of  $j_x$  and  $j_y$  is only  $2 \text{ kN/m}^3$  and  $0.2 \text{ kN/m}^3$ , respectively. And it seems that the distribution of  $j_y$  in the seabed foundation has no clear relation with the wave profile. The wave-induced vertical seepage force  $j_z$  is huge, and is the dominant factor for the seabed liquefaction. Its magnitude can reach up to  $30 \text{ kN/m}^3$ , which is much greater than  $9.81 \text{ kN/m}^3$ . At time  $t=60$  s, a wave trough arrives at the caisson breakwater;  $j_z$  near to the caisson breakwater is upward. The momentary liquefaction in this zone is most likely to occur. At time  $t=64$  s, a wave crest arrives at the caisson breakwater;  $j_z$  is downward. The seabed foundation in this zone is impossible to liquefy transiently.

Fig. 14 shows the predicted momentary liquefaction zones in the seabed foundation under the 3D wave loading in one typical wave period from  $t=60$  s to  $t=68$  s. Comparing the distribution of the liquefaction zones shown in Fig. 14 with the wave profile shown in Fig. 3, and with the distribution of the vertical seepage force  $j_z$  shown in Fig. 13, it is found that the momentary liquefaction indeed can only appear in the zones where the  $j_z$  is upward and under wave troughs. At time  $t=60$  s, a wave trough arrives at the caisson breakwater. The seabed foundation near to the front lateral side, and close to the breakwater head liquefies. This liquefaction may result in the collapse or tilt of the caisson breakwater. At time

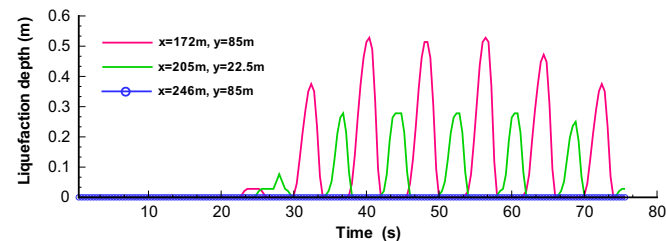


Fig. 15. Historical curve of the liquefaction depth at three typical positions.

$t=64$  s, a wave crest arrives at the caisson breakwater. The vertical seepage force  $j_z$  is downward, which makes the soil particles near to the caisson breakwater contact more densely. An important phenomenon observed in Fig. 14 is that the seabed foundation behind the caisson breakwater does not liquefy in the all time. This phenomenon indicates again that the breakwater has effectively protected the seabed and coastline behind it. The area of liquefaction zone induced by the standing wave in front of the caisson breakwater is much greater than that induced by the progressive wave. The liquefaction zones induced by the standing wave and progressive wave connect together sometimes, separate at other times.

The wave-induced liquefaction depth in the seabed foundation is an important parameter for coastal engineers involved in design of a marine structure. Fig. 15 demonstrates the time history of the liquefaction depth in the seabed foundation at three typical positions. It is found that the maximum depth of liquefaction zone in front of the breakwater is about  $0.528 \text{ m}$ , which is greater than that induced by the progressive wave ( $0.278 \text{ m}$ ). The liquefaction depth behind the caisson breakwater is always 0.

## 7. Parametric study

### 7.1. Effect of wave and soil characteristics

In the practice of offshore engineering, the porous seabed chosen as the foundation of marine structures is different from

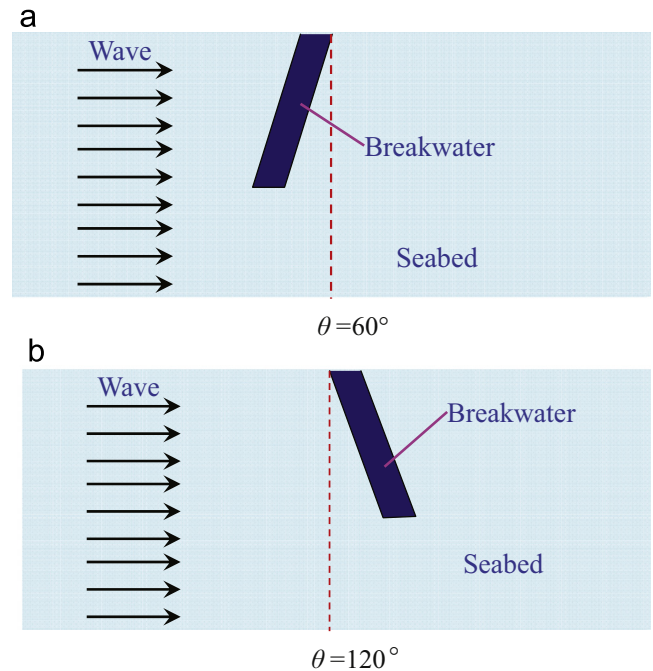


Fig. 16. Top-view of the breakwater, seabed and ocean wave system for  $\theta = 60^\circ$  and  $\theta = 120^\circ$ .

Table 2

Effect of wave and soil characteristics on the wave-induced maximum liquefaction depth in seabed foundation in front of the caisson breakwater.

Wave characteristics						Soil characteristics					
$H$ (m)	$d_{lique}$ (mm)	$T$ (s)	$d_{lique}$ (mm)	$d$ (m)	$d_{lique}$ (mm)	$E$ (MPa)	$d_{lique}$ (mm)	$k$ (m/s)	$d_{lique}$ (mm)	$S_r$ (%)	$d_{lique}$ (mm)
0.5	0.028	6	0.278	8	1.225	10	0.528	$10^{-7}$	0.528	95	0.778
1.5	0.528	8	0.528	10	0.528	20	0.528	$10^{-5}$	0.528	98	0.528
2.5	0.972	10	0.778	12	0.375	100	0.778	$10^{-3}$	0.028	100	0.0

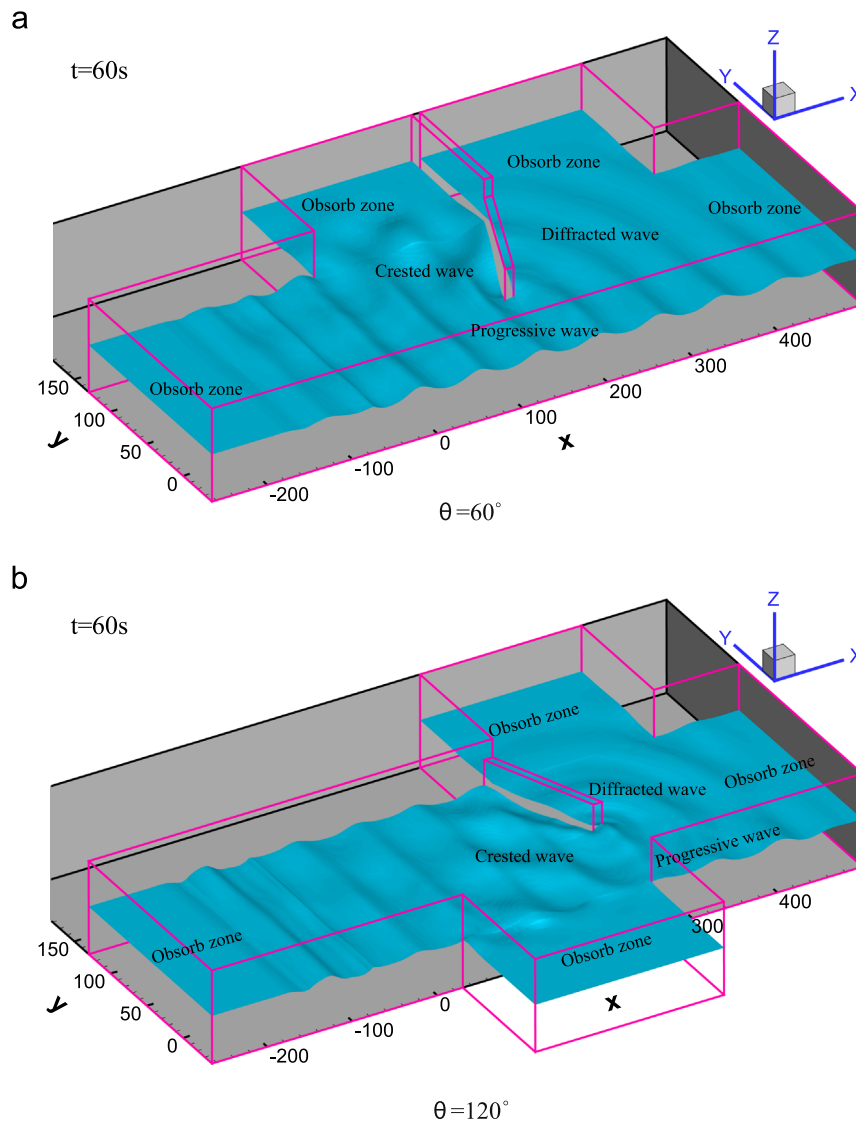


Fig. 17. Wave profile around the breakwater at a typical time for  $\theta = 60^\circ$  and  $\theta = 120^\circ$ . The position of the wave maker is at  $x = 0$  m.

cases to cases. It results in the property parameters of seabed foundation being various. How the wave characteristics and seabed properties affect the wave–seabed–breakwater interaction is an interesting topic for coastal engineers. Here, the wave-induced maximum liquefaction depth in the region in front of the caisson breakwater is taken as the representative quantity to investigate the effect of wave and soil characteristics on the wave–seabed–breakwater interaction.

Table 2 lists the wave-induced maximum liquefaction depth ( $d_{lique}$ ) in the seabed foundation in front of the caisson breakwater for different soils and wave characteristics. The standard parameters used here are the same with that listed in Table 1. When investigating the effect of one of those parameters, the other parameters are kept the same with the standard parameters. In Table 2, it is found that the maximum wave-induced liquefaction depth is mainly dependent on wave height, wave period, water depth, permeability and saturation of seabed. Young's modulus of seabed only could insignificantly affect the maximum liquefaction depth. The maximum liquefaction depth is proportional to the wave height and wave period and Young's modulus of seabed; and inversely proportional to water depth, permeability and saturation of seabed.

## 7.2. Effect of breakwater's direction

In offshore environment, caisson breakwater is not always perpendicular with incident wave. The angle between the caisson breakwater and incident wave (defined as  $\theta$ ) would be an important factor for the wave–seabed–structures interaction. In this section, the effect of breakwater's direction on the wave-induced dynamics of breakwater and seabed is investigated. Except for the configuration  $\theta = 90^\circ$ , other two configurations  $\theta = 60^\circ$  and  $\theta = 120^\circ$  are taken as the typical cases (see Fig. 16).

Undoubtedly, the direction of caisson breakwater relative to incident wave has significant effect on the wave field around the caisson breakwater. If the caisson breakwater is oblique with the incident wave, crested wave in front of the breakwater is formed, rather than standing wave. Regardless of standing wave or crested wave in front of the breakwater, there is still some wave energy passing through the breakwater in the form of progressive wave. Then the diffracted wave is formed behind the breakwater. Fig. 17 illustrates the wave profile around the breakwater at a typical time for the two configurations  $\theta = 60^\circ$  and  $\theta = 120^\circ$ . Comparing Figs. 17 and 3, it is found that the wave profiles around the caisson breakwater are indeed significantly different for the three

configurations. In the configurations  $\theta = 60^\circ$  and  $\theta = 120^\circ$ , crested wave in front of the breakwater is formed.

Different wave fields around the caisson breakwater certainly will result in different responses of the breakwater and its seabed foundation. First of all, the wave-induced force on the caisson breakwater would be significantly different. Fig. 18 demonstrates the wave-induced force acting on the front lateral side of the caisson breakwater in 1 m length. It is easy to find that the wave-induced force acting on breakwater is greatest if the incident wave is normal to the breakwater. In the case of  $\theta = 60^\circ$  and  $\theta = 120^\circ$ , the wave-induced force on the breakwater is only about half of that when  $\theta = 90^\circ$ . It means that the normal incident wave is most dangerous for the stability of breakwater.

Corresponding to the significant difference of the wave-induced force on the breakwater, the dynamic response of the caisson breakwater is also significantly different. Fig. 19 illustrates the wave-induced displacements of the caisson breakwater. In Fig. 19, it is found that the horizontal displacement  $u_s$  is greatest when  $\theta = 90^\circ$ , reaching up to 30 mm; and  $u_s$  when  $\theta = 60^\circ$  or  $\theta = 120^\circ$  is also only about half of that when  $\theta = 90^\circ$ . The displacement in the y direction  $v_s$  is apparently small when  $\theta = 90^\circ$ , only about 1.0 mm; while,  $v_s$  is relatively great when  $\theta = 60^\circ$  or  $\theta = 120^\circ$ , reaches up to 10 mm. For vertical displacement  $w_s$ , it is much greater when  $\theta = 90^\circ$  than that when  $\theta = 60^\circ$  or  $\theta = 120^\circ$ . It is noted here that the final settlement of caisson breakwater is also a little greater when  $\theta = 90^\circ$  than that when  $\theta = 60^\circ$  or  $\theta = 120^\circ$ . From the point of view of engineering experience, the excessive horizontal displacement  $u_s$  and vertical displacement  $w_s$  would result in the tilting and collapse of breakwater. Therefore, the obliquely incident wave maybe the best choice for the breakwater in design.

Fig. 20 shows the comparison of the wave-induced pressure acting on the seabed at three typical positions. As illustrated in

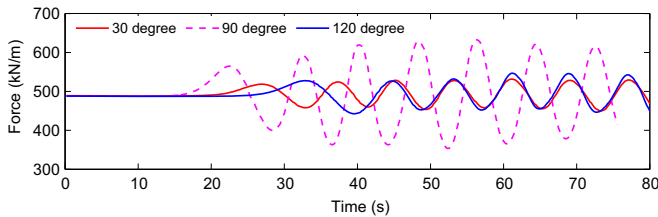


Fig. 18. Wave-induced force acting on the front lateral side of caisson breakwater in 1 m length.

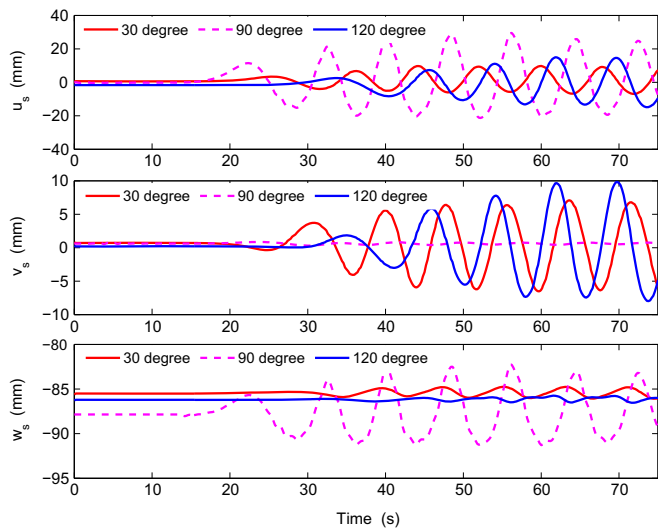


Fig. 19. Wave-induced displacements of caisson breakwater under wave loading.

Fig. 20, the difference of the wave-induced water pressure acting on the seabed foundation is not as significant as the wave-induced force acting on the breakwater. For the seabed in front of the breakwater, the amplitude of the wave-induced pressure when  $\theta = 120^\circ$  is a little smaller than that when  $\theta = 60^\circ$  and  $\theta = 90^\circ$ . For the seabed near to the breakwater head, the wave-induced pressure on the seabed is basically the same except the obvious phase difference. For the seabed behind the breakwater, the wave-induced pressure on the seabed when  $\theta = 120^\circ$  is a little greater than that when  $\theta = 60^\circ$  and  $\theta = 90^\circ$ . As a whole, the difference of wave-induced pressure acting on the seabed foundation is insignificant.

Although the wave-induced water pressure acting on the seabed foundation at the three typical positions is not significantly different for the three configurations, the wave-induced pore pressure in the seabed foundation is significantly different. Fig. 21 shows the wave-induced maximum pore pressure response in the seabed at the same three typical positions. It is found that the seabed response in front of the caisson breakwater is significantly different for the three configurations. The response of the seabed foundation is most intensive when  $\theta = 90^\circ$ . In the seabed near to the breakwater head, the seabed responses when  $\theta = 90^\circ$  and  $\theta = 120^\circ$  are basically the same, but a little greater than that when  $\theta = 60^\circ$ . In the seabed behind the breakwater, the seabed response when  $\theta = 90^\circ$  is greatest. These results also indicate that the normal incident wave is most dangerous for the stability of seabed foundation.

Wave-induced liquefaction in the seabed foundation is another important issue needed to be considered. Fig. 22 demonstrates the wave-induced liquefaction depth in the seabed foundation at the three typical positions. It is easy to find that the wave-induced liquefaction depth in front of the breakwater in the three configurations has the following sequence:  $d_{Lique-90} > d_{Lique-120} > d_{Lique-60}$ . In the seabed near to the breakwater head, the liquefaction depth has another sequence:  $d_{Lique-120} > d_{Lique-90} \geq d_{Lique-60}$ . In the seabed behind the breakwater, the liquefaction cannot occur in any configuration.

### 8. Conclusions

In this study, wave-induced dynamics of a caisson breakwater, and its very dense elastic seabed foundation is investigated comprehensively adopting the developed 3D integrated numerical model for FSSI. The computational results show that the interaction (except scouring) between ocean wave, offshore breakwater and its dense seabed foundation can be clearly and effectively

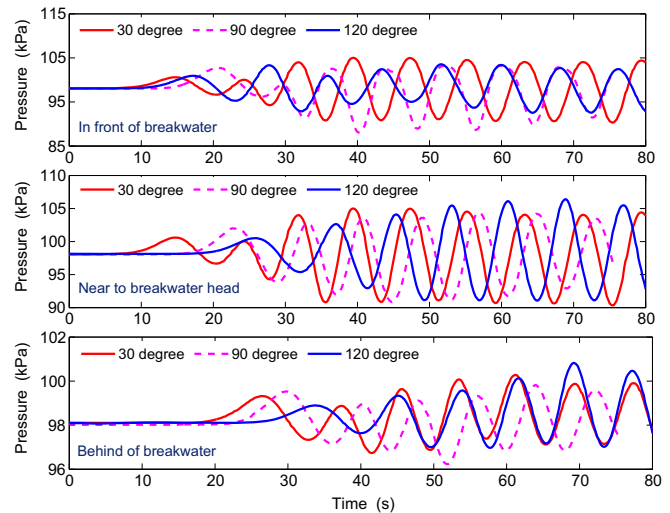


Fig. 20. Wave-induced pressure acting on seabed at typical positions.

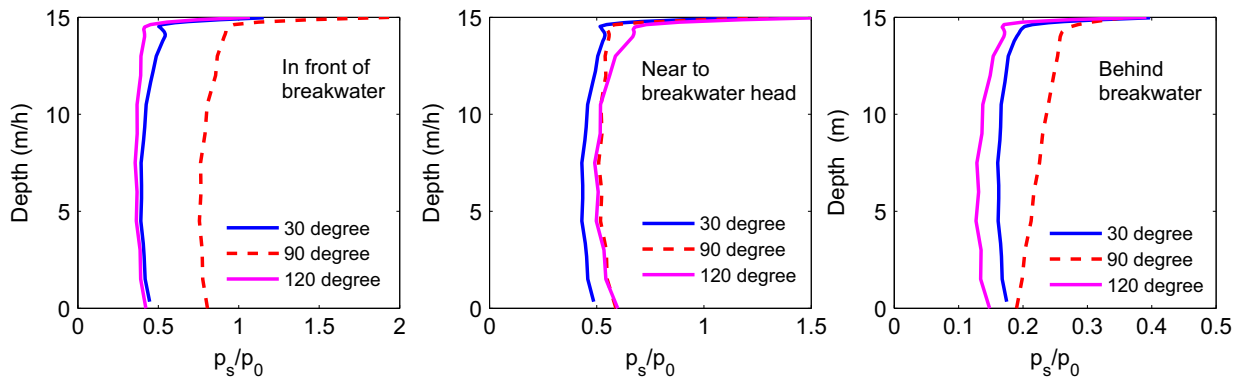


Fig. 21. Wave-induced maximum pore pressure response in seabed ( $p_0$  is the maximum linear wave-induced pressure,  $p_0 = \frac{\gamma_w H}{2 \cosh \pi d}$ ).

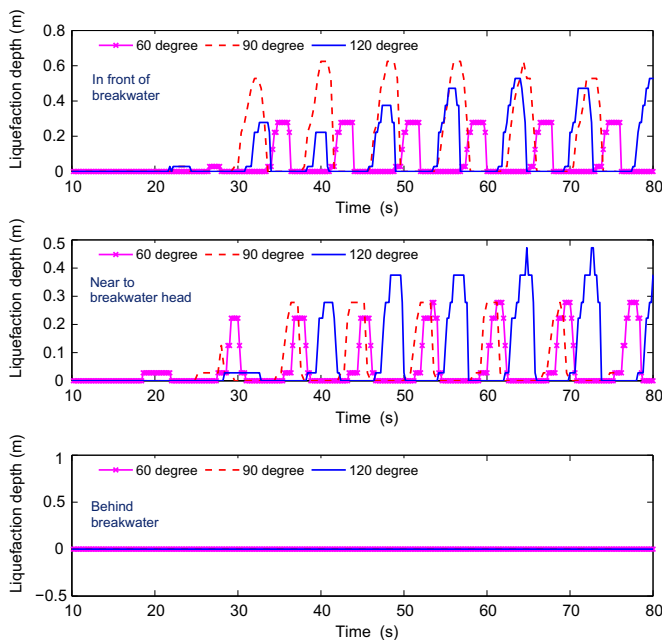


Fig. 22. Wave-induced liquefaction depth at typical positions in the seabed foundation.

captured by the integrated model FSSI-CAS 3D. This developed integrated numerical model would be a promising aided tool for ocean engineers to predict the dynamics and stability of offshore structures in design stage. Based on the results presented, the following conclusions are drawn:

1. In the interaction process between wave, seabed and caisson breakwater, there are three types of waves around the breakwater head: standing wave in front of the breakwater, progressive wave near to the breakwater head, and diffracted wave behind the breakwater. The 3D wave applies huge force on the front lateral side of the caisson breakwater, which is significantly greater than that on the rear lateral side of the breakwater. Under the 3D wave loading, the caisson breakwater sways accordingly.
2. Seabed response to 3D ocean wave at different regions around the breakwater head is significantly different. The seabed response in front of the caisson breakwater is strongest; while it is weakest behind the breakwater.
3. Under 3D ocean wave loading, momentary liquefaction could occur in dense seabed foundation in front of and near to the caisson breakwater. However, it is impossible for the seabed

foundation behind the caisson breakwater to liquefy due to the effective protection provided by the caisson breakwater.

4. Parametric study indicates that the maximum liquefaction depth in front of the caisson breakwater is mainly dependent on wave height, wave period, water depth, permeability and saturation of seabed. Young's modulus of the seabed could only insignificantly affect the maximum liquefaction depth. The direction of breakwater also significantly affects the interaction process between the wave, seabed and breakwater. When the breakwater is normal to incident wave, the maximum liquefaction depth in front of the breakwater is greatest, because the standing wave is formed due to the fact that the normal incident wave is nearly completely reflected by the breakwater.

**Acknowledgments**

Dr Ye Jianhong appreciates the financial funding support from National Natural Science Foundation of China under Project no. 41472291. Prof. Wang and Prof. Zhu thank the financial support from Chinese 973 Project: Evolutionary Trends and Sustainable Utilization of Coral Reefs in the South China Sea (2013CB956104). Dr Ye and Prof. Jeng are grateful for the financial support from EPSRC#EP/G006482/1. Dr Ye also appreciates the funding support of Overseas Research Student Award from Scottish Government, UK.

**References**

Carman, P.C., 1937. Fluid flow through granular beds. *Trans. Inst. Chem. Eng.* 15:150–66

Chung, S.G., Kim, S.K., Kang, Y.J., Im, J.C., Prasad, K.N., 2006. Failure of a breakwater founded on a thick normally consolidated clay layer. *Géotechnique* 56 (3), 393–409.

DeGroot, M.B., Kudella, M., Meijers, P., Oumeraci, H., 2006. Liquefaction phenomena underneath marine gravity structures subjected to wave loads. *J. Waterway Port Coast. Ocean Eng. ASCE* 132 (4), 325–335.

Franco, L., 1994. Vertical breakwaters: the Italian experience. *Coast. Eng.* 22 (1–2), 31–55.

Higuera, P., Lara, J.L., Losada, I.J., 2014a. Three-dimensional interaction of waves and porous coastal structures using Openfoam. Part I: formulation and validation. *Coast. Eng.* 83, 243–258.

Higuera, P., Lara, J.L., Losada, I.J., 2014b. Three-dimensional interaction of waves and porous coastal structures using Openfoam. Part II: application. *Coast. Eng.* 83, 259–270.

Hsu, J.R., Jeng, D.S., 1994. Wave-induced soil response in an unsaturated anisotropic seabed of finite thickness. *Int. J. Numer. Anal. Methods Geomech.* 18 (11), 785–807.

Hsu, T.J., Sakakiyama, T., Liu, P.L.F., 2002. A numerical model for wave motions and turbulence flows in front of a composite breakwater. *Coast. Eng.* 46, 25–50.

- Hur, D.S., Kim, C.H., Yoon, J.S., 2010. Numerical study on the interaction among a nonlinear wave, composite breakwater and sandy seabed. *Coast. Eng.* 57 (10), 917–930.
- Jeng, D.S., Cha, D.H., Lin, Y.S., Hu, P.S., 2001. Wave-induced pore pressure around a composite breakwater. *Ocean Eng.* 28 (10), 1413–1435.
- Jeng, D.-S., Ye, J.H., Zhang, J.-S., Liu, P.-F., 2013. An integrated model for the wave-induced seabed response around marine structures: model, verifications and applications. *Coast. Eng.* 72 (1), 1–19.
- Kirca, V., Sumer, B., Fredsoe, J., 2013. Residual liquefaction of seabed under standing waves. *J. Waterway Port Coast. Ocean Eng.* 139 (6), 489–501.
- Kudella, M., Oumeraci, H., Groot, M.B.D., Meijers, P., 2006. Large-scale experiments on pore pressure generation underneath a caisson breakwater. *J. Waterway Port Coast. Ocean Eng.* 132 (4), 310–324.
- Lee, J.F., Lan, Y.J., 2002. On waves propagating over poro-elastic infinite seabed. *Ocean Eng.* 29 (8), 931–946.
- Lee, T.C., Tsai, C.P., Jeng, D.S., 2002. Ocean wave propagating over a porous seabed of finite thickness. *Ocean Eng.* 29, 1577–1601.
- Lin, Z.P., Liu, P.L.-F., 1999. Internal wave-maker for Navier–Stokes equations models. *J. Waterway Port Coast. Ocean Eng.* 99 (4), 207–215.
- Mase, H., Sakai, T., Sakamoto, M., 1994. Wave-induced porewater pressure and effective stresses around breakwater. *Ocean Eng.* 21 (4), 361–379.
- Miyamoto, J., Sassa, S., Sekiguchi, H., 2004. Progressive solidification of a liquefied sand layer during continued wave loading. *Géotechnique* 54 (10), 617–629.
- Mizutani, N., Mostarfa, A., Iwata, K., 1998. Nonlinear regular wave, submerged breakwater and seabed dynamic interaction. *Coastal Eng.* 33, 177–202.
- Mizutani, N., Mostafa, A.M., Iwata, K., 1999. Numerical modeling of nonlinear interaction between wave and composite breakwater over sand bed. *J. Hydraul. Coast. Environ. Eng.* JSCE 614 (II-14), 121–133.
- Okusa, S., 1985. Wave-induced stress in unsaturated submarine sediments. *Géotechnique* 35 (4), 517–532.
- Truchas, 2009. TRUCHAS Physics and Algorithms. Los Alamos National Laboratory, version-2.5.3 edition.
- Tsai, C.P., Lee, T.L., Hsu, J., 2000. Effects of wave nonlinearity on the standing wave-induced seabed response. *Int. J. Numer. Anal. Method Geomech.* 24 (11), 869–892.
- Tsai, C.P., 1995. Wave-induced liquefaction potential in a porous seabed in front of a breakwater. *Ocean Eng.* 22 (1), 1–18.
- Ulker, M.B.C., Rahman, M.S., Guddati, M.N., 2009. Wave-induced dynamic response and instability of seabed around caisson breakwater. *Ocean Eng.* 37 (17–18), 1522–1545.
- Ulker, M.B.C., Rahman, M.S., Guddati, M.N., 2012. Breaking wave-induced response and instability of seabed around caisson breakwater. *Int. J. Numer. Anal. Methods Geomech.* 36 (3), 362–390.
- Yamamoto, T., Koning, H., Sellmeijer, H., Hijum, E.V., 1978. On the response of a poro-elastic bed to water waves. *J. Fluid Mech.* 87 (1), 193–206.
- Ye, J.H., Jeng, D.-S., 2013. Earthquake induced dynamic response of 3d poro-elastic unsaturated seabed under a rubble mound breakwater. *Soil Dyn. Earthq. Eng.* 44 (1), 14–26.
- Ye, J.H., Jeng, D.-S., Chan, A.H.C., 2012. Consolidation and dynamics of 3D unsaturated porous seabed under rigid caisson breakwater loaded by hydrostatic pressure and wave. *Sci. China-Technol. Sci.* 55 (8), 2362–2376.
- Ye, J.H., Jeng, D.-S., Wang, R., Zhu, C.Q., 2013a. A 3-D semi-coupled numerical model for fluid–structures–seabed–interaction (FSSI-CAS 3D): model and verification. *J. Fluids Struct.* 40, 148–162.
- Ye, J.H., Jeng, D.-S., Wang, R., Zhu, C.-Q., 2013b. Numerical study of the stability of breakwater built on sloped porous seabed under tsunami loading. *Appl. Math. Model.* 37, 9575–9590.
- Ye, J.H., Jeng, D.-S., Wang, R., Zhu, C.-Q., 2013c. Validation of a 2D semi-coupled numerical model for Fluid–Structures–Seabed interaction. *J. Fluids Struct.* 42, 333–357.
- Ye, J.H., Jeng, D.-S., Liu, P.L.-F., Chan, A.H.C., Wang, R., Zhu, C.-Q., 2014. Breaking wave-induced response of composite breakwater and liquefaction of seabed foundation. *Coastal Eng.* 85, 72–86.
- Ye, J.H., Jeng, D.-S., Wang, R., Zhu, C.-Q., 2015. Numerical simulation of wave-induced dynamic response of poro-elasto-plastic seabed foundation and composite breakwater. *Appl. Math. Model.* 39, 322–347.
- Ye, J.H., 2012a. 3D liquefaction criteria for seabed considering the cohesion and friction of soil. *Appl. Ocean Res.* 37, 111–119.
- Ye, J.H., 2012b. Numerical Analysis of Wave–Seabed–Breakwater Interactions (Ph.D. thesis), University of Dundee, Dundee, UK.
- Ye, J.H., 2012c. Seismic response of poro-elastic seabed and composite breakwater under strong earthquake loading. *Bull. Earthq. Eng.* 10 (5), 1609–1633.
- Zhang, F.G., Ge, Z.J., 1996. A study on some causes of rubble mound breakwater failure. *China Ocean Eng.* 10 (4), 473–481.
- Zienkiewicz, O.C., Chang, C.T., Bettess, P., 1980. Drained, undrained, consolidating and dynamic behaviour assumptions in soils. *Géotechnique* 30 (4), 385–395.